Production cross sections of neutron-rich nuclides near the $N = 126$ neutron-shell closure from 1000 MeV/u ^{208}Pb on ^{9}Be

Suraj Kumar Singh,[1,2,3,*] Emma Haettner,[1,†] Christine Hornung,[1] Gee Bartram,[4] Timo Dickel,[1,2] Justus M. Eder,[1] Nicolas Hubbard,[1,5] Zsolt Podolyák,[4] Rinku Prajapat,[1,6] José Luis Rodríguez-Sánchez,[7,8] Christoph Scheidenberger,[1,2,3] Yoshiki K. Tanaka,[9] Jianwei Zhao,[1] Jaime Acosta,[10] Guler Aggez,[1] Muneerah Al-Aqeel,[11] Betool Alayed,[12,13] Helena M. Albers,[1] Ahmed Alharbi,[12,13] Sultan Alhomaidhi,[1,5,14,15] Faraz Amjad,[1] Tugba Arici,[1] Michael Armstrong,[1] Martin Bajzek,[1] Akashrup Banerjee,[1] Giovanna Benzoni,[16] Nara Singh Bondili,[17] Alison Bruce,[18] Carlo Bruno,[19] Jamie Chadderton,[13] Zhiqiang Chen,[1] Fabio C. L. Crespi,[16,20] Biswajit Das,[21] Santwana Dubey,[1] Joachim Enders,[5,15] Martina Feijoo-Fontán,[8] Carlos Ferrera,[10] Eugenio R. Gamba,[16,20] Zhuang Ge,[1] Hans Geissel,[1,2,‡] Jürgen Gerl,[1] Pavel Golubev,[22,§] Antia Graña-González,[8] Magda Górska,[1] Andrea Gottardo,[23] Tuomas Grahn,[24,25] Oscar Hall,[19] Muhsin N. Harakeh,[26] Laura Harkness-Brennan,[13] Yuliia Hrabar,[22,‖] Shaheen Jazrawi,[4] Philipp R. John,[5] Calum E. Jones,[4] Dan Judson,[13] Andrea Jungclaus,[10] Nasser Kalantar-Nayestanaki,[26] Erika Kazantseva,[1] Ronja Knöbel,[1] Pavlos Koseoglou,[5] Aleksandrina Kosir,[1,27] Gregor Kosir,[28] Daria Kostyleva,[1] Marc Labiche,[29] Eva Lovsin,[28,30] Radomira Lozeva,[31] Adam McCarter,[13,¶] Daniele Mengoni,[32,33] Michal Mikolajczuk,[34] Benedicte Million,[16] Andrew K. Mistry,[1] Ana I. Morales,[35] David J. Morrissey,[36,1] Ivan Mukha,[1] Gopal Mukherjee,[37] Sonja E. A. Orrigo,[35] Robert Page,[13] Rudrajyoti Palit,[21] Philippos Papadakis,[29] Tom G. Parry,[4] Sorin Pascu,[4] Norbert Pietralla,[5,15] Stephane Pietri,[1] Wolfgang R. Plaß,[1,2] Marta Polettini,[16,20] Patrick H. Regan,[4,38] Ellis Rintoul,[13] Elena Rocco,[1] David Rodriguez-Garcia,[35] Heidi Rösch-Kabadayi,[1,5,15] Pratap Roy,[37,1] Matthias Rudigier,[5] Dirk Rudolph,[22] Elif Sahin,[24] Luis Sarmiento Pico,[22] Maria-Magdalini Satrazani,[13,**] Min Si,[31] Ionut C. Stefanescu,[39,††] Jose Luis Tain,[35] Matjaz Vencelj,[28] Jelena Vesić,[28] Helmut Weick,[1] Volker Werner,[5] Oliver Wieland,[16] Kathrin Wimmer,[1] Jin Wu,[40] Yener Yasun,[41] and Guangxin Zhang[32]

(HISPEC/DESPEC Collaboration, Super-FRS Experiment Collaboration)

[1]*GSI Helmholtzzentrum für Schwerionenforschung GmbH, 64291 Darmstadt, Germany*

[2]*II. Physikalisches Institut, Justus-Liebig-Universität Gießen, 35392 Gießen, Germany*

[3]*Helmholtz Forschungsakademie Hessen für FAIR (HFHF), GSI Helmholtzzentrum für Schwerionenforschung GmbH, Campus Gießen, 35392 Gießen, Germany*

[4]*Department of Physics, University of Surrey, Guildford, Surrey GU2 7XH, United Kingdom*

[5]*Institut für Kernphysik, Technische Universität Darmstadt, 64289 Darmstadt, Germany*

[6]*Astronomy and Physics Department, Saint Mary's University, Halifax, Nova Scotia B3H 3C3, Canada*

[7]*CITENI, Campus Industrial de Ferrol, Universidade da Coruña, E-15403 Ferrol, Spain*

[8]*IGFAE, Universidade de Santiago de Compostela, E-15782 Santiago de Compostela, Spain*

[9]*RIKEN Cluster for Pioneering Research, RIKEN, Wako, Saitama 351-0198, Japan*

[10]*Instituto de Estructura de la Materia, Consejo Superior de Investigaciones Científicas (CSIC), Madrid, Spain*

[11]*College of Science, Imam Mohammad Ibn Saud Islamic University (IMSIU), Riyadh, Saudi Arabia*

[12]*Department of Physics, College of Science, Qassim University, Buraydah 51452, Saudi Arabia*

[13]*Department of Physics, University of Liverpool, Liverpool L69 7ZE, United Kingdom*

[14]*King Abdulaziz City for Science and Technology (KACST), Riyadh 11442, Saudi Arabia*

[15]*Helmholtz Forschungsakademie Hessen für FAIR (HFHF), GSI Helmholtzzentrum für Schwerionenforschung GmbH, Campus Darmstadt, 64289 Darmstadt, Germany*

[*]Contact author: s.k.singh@gsi.de

[†]Contact author: e.haettner@gsi.de

[‡]Deceased.

[§]Present address: Detector Group, European Spallation Source ERIC, 221 00 Lund, Sweden.

[‖]Present address: Nuclear Science Division, Lawrence Berkeley National Laboratory, Berkeley, CA 94720, USA.

[¶]Present address: Van Swinderen Institute for Particle Physics and Gravity, University of Groningen, Groningen, 9747AA, The Netherlands.

[**]Present address: TRIUMF, 4004 Wesbrook Mall, Vancouver, V6T 2A3 BC, Canada.

[††]Present address: Institut für Kernphysik, Technische Universität Darmstadt, 64289 Darmstadt, Germany.

Published by the American Physical Society under the terms of the Creative Commons Attribution 4.0 International license. Further distribution of this work must maintain attribution to the author(s) and the published article's title, journal citation, and DOI.

[16]*Istituto Nazionale di Fisica Nucleare (INFN), Sezione di Milano, 20133 Milano, Italy*
[17]*School of Computing, Engineering and Physical Sciences, University of the West of Scotland, Paisley PA1 2BE, United Kingdom*
[18]*School of Architecture, Technology and Engineering, University of Brighton, Brighton BN2 4GJ, United Kingdom*
[19]*School of Physics and Astronomy, University of Edinburgh, Edinburgh EH9 3FD, United Kingdom*
[20]*Dipartimento di Fisica, Università degli Studi di Milano, 20133 Milano, Italy*
[21]*Department of Nuclear and Atomic Physics, Tata Institute of Fundamental Research (TIFR), Mumbai 400005, India*
[22]*Department of Physics, Lund University, 221 00 Lund, Sweden*
[23]*Istituto Nazionale di Fisica Nucleare (INFN), Laboratori Nazionali di Legnaro, 35020 Legnaro, Italy*
[24]*Department of Physics, University of Jyväskylä, 40014 Jyväskylä, Finland*
[25]*Helsinki Institute of Physics, PO Box 64, FI-00014 University of Helsinki, Finland*
[26]*ESRIG, University of Groningen, 9747 AA Groningen, The Netherlands*
[27]*Institute for Nuclear Physics, University of Cologne, 50937 Köln, Germany*
[28]*Jožef Stefan Institute, 1000 Ljubljana, Slovenia*
[29]*STFC Daresbury Laboratory, Daresbury, Warrington WA4 4AD, United Kingdom*
[30]*Faculty of Mathematics and Physics, University of Ljubljana, 1000 Ljubljana, Slovenia*
[31]*Université Paris-Saclay, IJCLab, CNRS/IN2P3, F-91405 Orsay, France*
[32]*Dipartimento di Fisica e Astronomia, Università degli Studi di Padova, 35131 Padova, Italy*
[33]*Istituto Nazionale di Fisica Nucleare (INFN), Sezione di Padova, 35131 Padova, Italy*
[34]*Faculty of Physics, University of Warsaw, 02-093 Warsaw, Poland*
[35]*Instituto de Física Corpuscular (IFIC), CSIC-Universitat de València, 46980 Paterna, Spain*
[36]*Department of Chemistry, Michigan State University, East Lansing, Michigan 48824, USA*
[37]*Variable Energy Cyclotron Centre (VECC), Kolkata 700064, India*
[38]*National Physical Laboratory, Teddington TW11 0LW, United Kingdom*
[39]*Horia Hulubei National Institute for R&D in Physics and Nuclear Engineering (IFIN-HH), 077125 Măgurele, Romania*
[40]*Department of Physics and Astronomy, Michigan State University, East Lansing, Michigan 48824, USA*
[41]*Department of Physics, Istanbul University, 34134 Istanbul, Turkey*

(Received 16 April 2026; accepted 8 September 2026; published 16 October 2026)

The production cross sections of neutron-rich nuclides near the $N = 126$ neutron shell closure have been measured for the elements ranging from tungsten ($Z = 74$) to gold ($Z = 79$) in the fragmentation of a 1000 MeV/u ^{208}Pb beam on a ^{9}Be target. Several cross sections, namely those for $^{196-199}$W, $^{199-201}$Re, and $^{202-203}$Os, were determined for the first time with this projectile-target combination. The results are compared with the predictions of several nuclear reaction models and semiempirical parametrizations; special attention is devoted to multiple proton-removal channels and the formation of nuclides with neutron number $N = 127$.

DOI: 10.1103/p27s-fp1j

I. INTRODUCTION

Beyond the stable nuclei, nuclear physics is constantly pushing the boundaries to investigate the vast and mainly unexplored realm of exotic nuclei. Although approximately 300 stable nuclides have traditionally served as basis for the development of nuclear theories, more than 3000 nuclides are currently known [1], and theoretical estimates indicate that there may be about 7000 bound nuclides up to element number 120 [2]. This immense, largely unexplored, nuclear landscape raises fundamental questions about the suitability of existing theoretical descriptions, which were primarily developed for nuclei around the β-stability line and those in its vicinity. This quest for exotic atomic nuclei has already led to the discovery of new chemical elements, novel structures and phenomena such as halo nuclei [3] and multiple-proton radioactivity [4], has unveiled deformation regions and unexpected single- or double-shell closures far from stability [5]. The current focus lies in understanding basic nuclear properties, such as shell structure, pairing, and deformation and how they evolve with extreme isospin. The structure of nuclei is expected to change significantly as the neutron and proton drip lines are approached, necessitating a re-evaluation and improvement of existing nuclear structure theories. Despite significant progress [1], the limits of nuclear existence are still being explored. The proton drip line has been experimentally reached for elements with atomic number $Z \lesssim 80$ [6], but the neutron drip line remains inaccessible, for all but the lightest elements. This poses a major experimental challenge and represents a key frontier in nuclear physics research.

Understanding the neutron-rich heavy nuclei is crucial for several reasons, including their significance for nuclear structure studies and their pivotal role in the astrophysical nucleosynthesis. The r-process, or rapid neutron-capture process, is believed to be responsible for the creation of approximately half of the elements heavier than iron in the Universe [7]. Knowledge of nuclear properties, particularly masses, β-decay half-lives, neutron-capture cross sections and fission barriers and yields of heavy neutron-rich nuclei far from stability is essential to model the r-process quantitatively. Regions like the r-process waiting point at neutron number

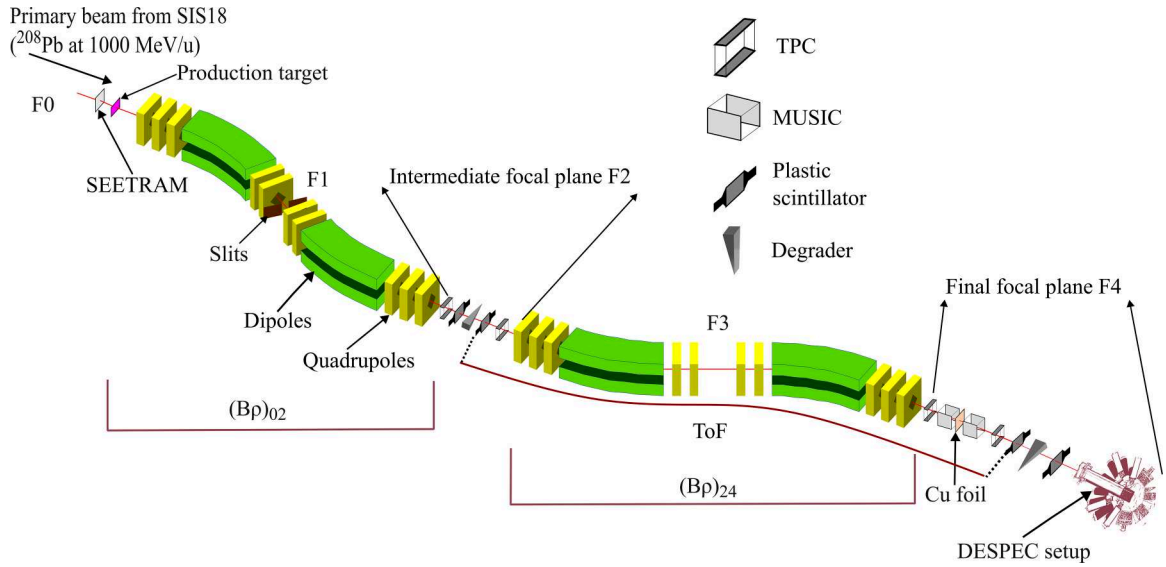


FIG. 1. Schematic layout of the FRS showing its focal planes F0–F4. The production target was located at F0; F1 and F3 were under vacuum; F2 was dispersive and F4 achromatic. Single particle detectors were placed in air gaps at F2 and F4, and the DESPEC setup was situated at F4. $(B\rho)_{02}$ and $(B\rho)_{24}$ are the magnetic rigidity of the separator in each section.

$N = 126$ are of specific interest, as they are crucial for the formation of the third r-process abundance peak at mass number $A \approx 195$ [7], but remain largely unexplored experimentally.

The production of unstable nuclei with sufficiently high yields to allow for experimental investigation, especially those with extremely short half-lives is a significant scientific and technological challenge. This endeavor requires methods for generating intense radioactive ion beams with two primary techniques being Isotope Separation On-Line (ISOL) and in-flight separation [8–11]. Investigating the key reaction mechanisms involved and understanding their features qualitatively and quantitatively is essential. The primary processes for producing exotic nuclei include fission, spallation and fragmentation. The latter are peripheral heavy-ion collisions at relativistic energies and interpreted as a two-step process [12]: a fast initial step (abrasion) leading to an excited prefragment, followed by a second step (ablation, evaporation, or fission) where the reaction residues are formed. Another important process at more central collisions, leading to higher excitation energies, is multi-fragmentation. Finally, charge-exchange reactions [13] can influence the final fragment yields.

In this article, the production cross sections of nuclides originating from 1000 MeV/u ^{208}Pb impinging onto a ^{9}Be target have been obtained for several neutron-rich nuclides, particularly those along the $N = 126$ closed shell. The experiment was carried out with the fragment separator (FRS) [14] located after the SchwerIonen Synchrotron (SIS18) at the GSI laboratory in Darmstadt, Germany.

II. EXPERIMENTAL PROCEDURE AND DATA ANALYSIS

Heavy neutron-rich nuclides were produced by fragmentation of a relativistic 1000 MeV/u ^{208}Pb beam on a beryllium target. The ^{208}Pb primary beam was accelerated in the SIS18 and extracted with extraction times varying dependent on fragment setting from 0.5 s to 5 s and intensities of up to 5×10^8 particles per spill, the total number of primary beam particles per setting is given in Sec. II B 1. The ^{9}Be production target, characterized by the GSI Target Laboratory [15], had a thickness of (2512 ± 25) mg/cm^2 located at the entrance (F0) of the FRS, see Fig. 1. It was backed with a 220 mg/cm^2 Nb stripper to maximize the fraction of fully ionized fragments. The target thickness corresponds to approximately 20% of the projectile range and the reaction probability for the primary beam was approximately 40%. The FRS was operated in an overall achromatic mode from target to the final focal plane F4 and with a dispersion of -6.8 cm/% at the intermediate focal plane F2. An energy-loss degrader made of 4500 mg/cm^2 Al was installed at F2. Isotopic separation was achieved by $B\rho - \Delta E - B\rho$ method [14]: the magnetic rigidity $B\rho$ of the fragments is analyzed in the first half of the separator, and their energy loss ΔE, which depends on their atomic number, mass number and velocity, is analysed with the second stage of the separator.

The main aim of the present experiment was nuclear-structure studies via decay spectroscopy [16] using the DESPEC setup [17] at the final focal plane F4 of the FRS. The experiment was performed with two different separator settings: one setting aimed at maximum transmission of the fully stripped ^{203}Ir passing through the separator at a magnetic rigidity $(B\rho)_{02} = 13.2224$ Tm and $(B\rho)_{24} = 9.5671$ Tm and the other setting at fully stripped ^{202}Os with $(B\rho)_{02} = 13.3486$ Tm and $(B\rho)_{24} = 9.7927$ Tm. The quantities $(B\rho)_{02}$ and $(B\rho)_{24}$ refer to the magnetic rigidities of the separator on its ion-optical axis between the focal planes from F0 to F2 and from F2 to F4, respectively. In the ^{202}Os setting, the fragment of interest was centered at F2 but off-set on purpose by 30 mm at F4 to allow for good transmission of other interesting nuclides to the final focus F4 for nuclear-spectroscopy studies. The slits at F1 were set to ± 35 mm to suppress fragments with momentum deviations

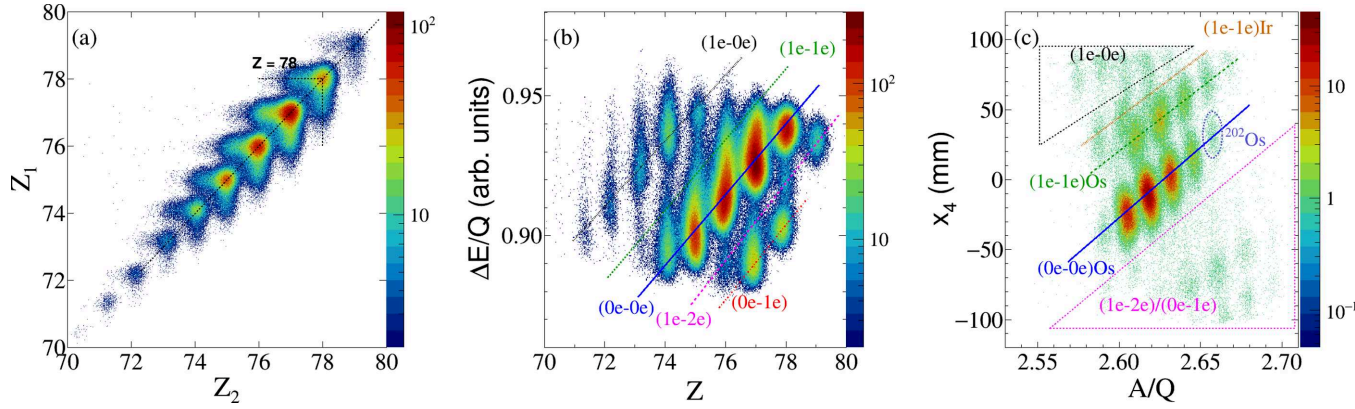


FIG. 2. (a) Plot showing the correlation between Z_1 and Z_2 measured by the two MUSICs at F4 for the ^{202}Os setting. Diagonal dashed line indicates ions fully ionized in both MUSICs. (b) Energy loss per charge Q of the fragment [see Eq. (1)] in the material and degrader at the F2 focal plane versus the measured atomic number Z of fragments for the ^{202}Os setting. Each diagonal set of blobs represents a different charge state configuration in the separator: fully ionized (0e-0e, blue solid line), hydrogen-like in both stages (1e-1e, green dashed line), hydrogen-like then fully ionized ion (1e-0e, black dotted line), fully ionized then hydrogen-like (0e-1e, red dash-dotted line), and first hydrogen-like and finally helium-like (1e-2e, magenta long-dashed line). (c) Plot of x_4 position at F4 versus A/Q for $Z = 76$ fragments. In this plot the (0e–0e) osmium isotopes (solid blue line) are clearly separated from the 1e–1e osmium isotopes (green long-dashed line). Hydrogen-like 1e–1e iridium (orange dotted line) and small contributions from other charge-state combinations (e.g., 1e–2e, 0e–1e, and 1e–0e) are also visible and well separated from the dominant band of (0e-0e) peaks. The position of ^{202}Os is highlighted for reference.

exceeding the momentum acceptance of the FRS as early as possible.

A. Particle identification

The unambiguous identification of projectile fragments was achieved in terms of both atomic number Z and mass number A event by event using the $B\rho - \Delta E^* -$ ToF method using the detector system shown in Fig. 1. The atomic number of the fragments was determined by measuring their energy deposition (ΔE^*) in a pair of multiple-sampling ionization chambers (MUSICs) located at the exit of the FRS at F4 [18]. Since ΔE^* depends on the ion velocity, a velocity correction was applied event-by-event to the measured ΔE^* signals. The velocity correction function was determined from measurements of the unreacted primary beam at three different well-defined velocities. The corrected energy-loss signals were then used to determine the corresponding charge of the ion, denoted as Z_1 and Z_2 for the two MUSIC detectors. For fully stripped ions, Z_1 and Z_2 correspond to the nuclear charge of the fragment.

A 90 mg/cm^2 thick Cu foil was placed between these two MUSICs to maximise the fraction of fully ionised ions. Plotting the Z_1 and Z_2 measurements of the two MUSICs versus each other, as shown in Fig. 2(a), results in wing pattern where the horizontal branch corresponds to ions that were fully ionised in the first MUSIC, while the vertical branch corresponds to ions fully ionized in the second MUSIC. Overlap between the wings occurs when ions are fully ionized in both MUSICs indicated by diagonal dashed line. The atomic number Z was determined from the calculated average of Z_1 and Z_2, both determined in MUSIC1 and MUSIC2, respectively, for $|Z_1 - Z_2| < 0.5$. In cases where $|Z_1 - Z_2| > 0.5$ the Z was calculated as the maximum of Z_1 and Z_2. A small amount of ions, up to 4%, are hydrogen or helium-like ions in both MUSICs. The fraction was determined by selection of the corresponding Z in Fig. 2(a). Projection of the selected Z onto the Z_1 and Z_2 axes yielded the probability for an ion to be detected as not fully ionized in each of the two MUSIC detectors. The probability of not being fully ionized in both MUSIC detectors is then calculated from these values. Events with an incorrect Z assignment were identified by analysis of their position at F4 and excluded from the subsequent analysis; see Fig. 2(c).

The mass-to-charge ratio (A/Q), where Q is the ionic charge number, was calculated using the measured $B\rho$ and the velocity of each ion. The $B\rho$ in the second half of the FRS was determined by the measured horizontal positions of the fragment at F2 (x_2) and at F4 (x_4), each measured with a pair of time projection chambers (TPCs) placed at F2 and F4 [19,20], combined with known ion-optical parameters and the central $(B\rho)_{24}$. The velocity was determined via time-of-flight (ToF) measurement between plastic-scintillator detectors placed at F2 and F4 [21] combined with position information at F2 and F4 to account for flight path-length differences from the central trajectory.

It is crucial to determine and distinguish between different ionic charge states to avoid misidentification. The energy loss ΔE of a fragment ion in the matter at F2 helps to resolve this ambiguity, as described in Refs. [22,23]

$$\Delta E = Qe \cdot c[(B\rho)_{02}/\beta_{02} - (B\rho)_{24}/\beta_{24}], \qquad (1)$$

where β_{02} and β_{24} are the velocities of the fragments in separator relative to the speed of light from F0 to F2 and from F2 to F4, respectively, e is the elementary charge, and c is the speed of light. The relative velocity β_{24} was calculated from the ToF measured using scintillator detectors placed at F2 and F4, and the β_{02} was determined from $(B\rho)_{02}$ and $(A/Q)_{02}$ assuming $(A/Q)_{02} = (A/Q)_{24}$. Figure 2(b) shows the measured energy loss per charge $\Delta E/Q$ versus the Z measured by the MUSICs

at F4 as described above. In this representation, the different charge state combinations are clearly visible.

Ions which undergo an ionic charge change between the two $B\rho$ sections of the FRS (i.e., at the central focal plane F2) are shifted off the main identification line in the $\Delta E/Q$ versus Z plane as shown in Fig. 2(b). In Fig. 2(b), each line represents a different charge state configuration. The solid blue line labeled (0e-0e) corresponds to fragments which were fully ionized in both $B\rho$ stages of FRS. The green dashed line labeled (1e-1e) represents fragments that passed through both stages of the FRS as hydrogen-like ions. The black dotted line labeled (1e-0e) corresponds to fragments which were hydrogen-like ions in the first stage and lost an electron at intermediate plane and traverse the second stage as fully ionized. This allows to disentangle ions which change in their charge state at F2 from those which do not change their charge state, and even provides a rough separation between the (0e-0e) and (1e-1e) ions. The Fig. 2(c) shows the x_4 position at F4 versus A/Q for a certain element, in this case osmium ($Z = 76$). This representation allows separation of the fully ionized (0e–0e) osmium isotopes, represented by a solid blue line, from the hydrogen-like (1e–1e) osmium isotopes, indicated by a green long-dashed line. A small fraction of hydrogen-like (1e–1e) iridium ions, indicated by orange dotted line, were also recorded as hydrogen-like ions in both MUSIC detectors.

Additional minor contributions from other charge-state combinations, such as (1e-2e) osmium or (0e-1e) osmium and iridium ions, are enclosed by a magenta dashed triangle in the lower right corner. The ions enclosed by a black dashed triangle in the upper left corner are small amounts of (1e–0e) osmium and rhenium ions and possibly also (0e-0e) platinum ions that were doubly charged in both MUSICs. The appearance of these minor charge-state combinations is the result of the wide gate applied on $Z = 76$ during selection in Fig. 2(b). This wide gate was necessary as the energy loss in the degrader was not sufficient for clear separation between (0e-0e) and (1e-1e) charge-state combinations. Similarly, due to the finite Z resolution, the gate also includes a small fraction of neighboring elements with $Z - 1$ and $Z + 1$. Finally, and after selecting the ions which were fully ionized in both sections F0-F2 and F2-F4 using the described method, the atomic number and mass number of fragments can be unambiguously determined. Figures 3(a) and 3(b) show, for the ^{203}Ir and the ^{202}Os setting, respectively, the resulting plots of atomic number Z versus the A/Q ratio. This unambiguous identification was confirmed independently through the well-established isomer-tagging method using the decay-spectroscopy setup at F4 mentioned earlier. Several previously reported isomeric states, including those in the $N = 126$ isotones ^{206}Hg [24], ^{205}Au [25], and ^{204}Pt [26] were measured.

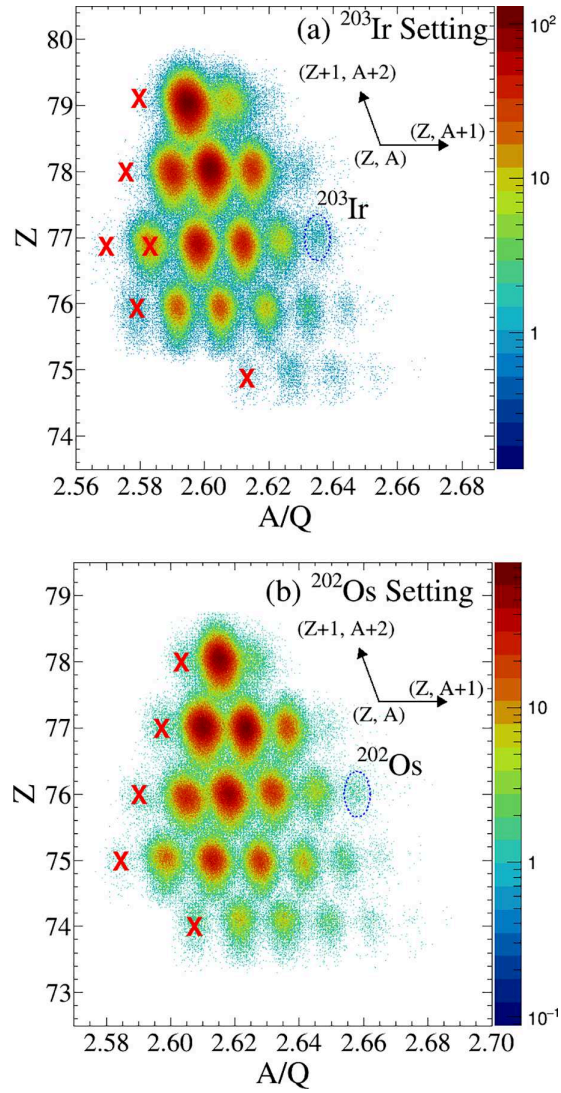


FIG. 3. Particle identification (PID) plot of the ions which were fully ionised in both stages of the separator, i.e., for which $Q = Z$. The plot shows the atomic number Z versus the A/Q ratio for (a) the ^{203}Ir setting and (b) the ^{202}Os setting. For clarity, the centered isotope is highlighted and labeled with its mass number. The arrows show the relations of atomic and mass numbers of the nuclides. The red crosses indicate those nuclides, for which ion-optical transmission was determined to be less than 10% and their production cross sections were not evaluated from this setting; for details see Sec. II B 3.

B. Determination of production cross sections

After obtaining the PID plots for both experiment settings and identifying Z and A, the production cross sections were determined according to the steps described in the following. The PID plots were projected individually for every element on the A/Q axis, resulting in yield distributions, which were then used to determine the number of observed counts N_f for every isotope of that element. Examples for the ^{202}Os setting are shown for rhenium ($Z = 75$) and tungsten ($Z = 74$) isotopes in Figs. 4(a) and 4(b), respectively. The spectra were fitted using a sum of Gaussian distributions. The area and centroid were treated as free fitting parameters. The width parameter was also a fit parameter, but was constrained to be the same for all isotopes within an isotopic chain. The number of counts for each isotope was then extracted from the fit of the corresponding individual Gaussian distribution. In a few cases, where only a small number of events was observed, the centroid of the corresponding peak was fixed. For comparison,

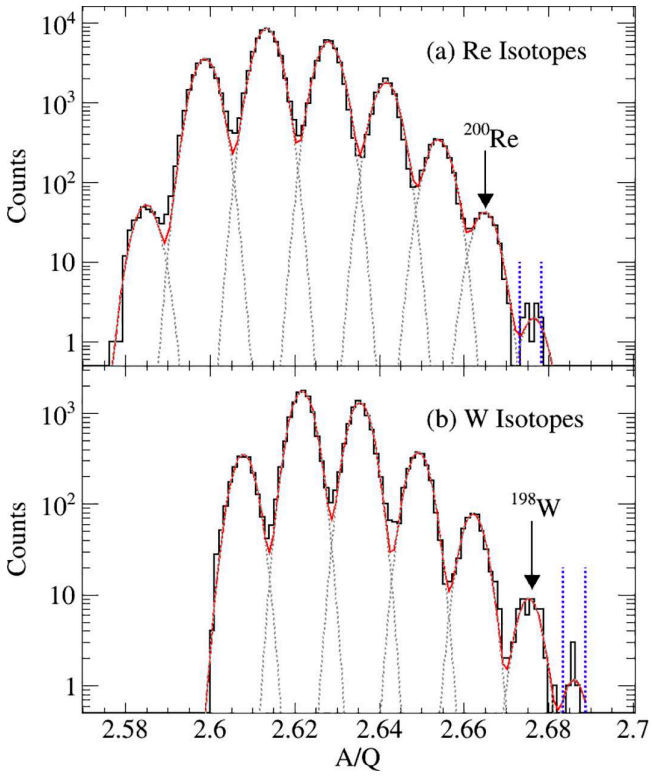


FIG. 4. A/Q spectra for (a) rhenium isotopes and (b) tungsten isotopes produced in the ^{202}Os setting. One isotope is labeled with an arrow for reference. The A/Q spectra were fitted with a sum of Gaussian distributions. In addition to the fit, the number of counts of the two peaks with smallest statistics was obtained by counting within the region indicated by blue dashed lines; for details see text.

events were also counted within the limits indicated by the dotted blue vertical lines, as indicated in Fig. 4. For these low-statistics cases, the counting and fitting methods agreed within 70%. For such nuclides, the counted number of events was used for the cross-section evaluation.

The production cross sections (σ) of each nuclide were determined using the following equation:

$$\sigma = \frac{N_f}{n_t \cdot \sum_{i=1}^{j} \frac{N^i_{\text{proj}}}{f^i_{DAQ} \cdot f^i_{\text{det}}}} \cdot f_{tr} \cdot f_q \cdot f_{rxn} \cdot f_{\text{target}}, \qquad (2)$$

where N_f is the measured yield at F4 and n_t the number of target atoms per unit area. Since the incident beam intensity from SIS18 varied during the experiment, the dead time of the data-acquisition system and the detector and reconstruction efficiencies also varied during data taking. Therefore, these time-dependent corrections were applied spill by spill as shown in Eq. (2), where j is the total number of spills, while N^i_{proj}, f^i_{DAQ}, and f^i_{det} represent the number of primary particles, the dead-time correction factor, and the correction factor for the combined detector and particle reconstruction efficiencies for the ith spill, respectively.

For the ^{203}Ir setting, the time-dependent corrections correspond to an overall factor of 2.0 ± 0.2, while for the ^{202}Os setting the corresponding factor amounts to 2.2 ± 0.2. The other factors of Eq. (2) take into account transmission losses due to geometrical limitations of apertures (f_{tr}), distribution over different ionic charge states (f_{q}), losses due to reactions in matter (f_{rxn}), multistep production probabilities in the Be production target as well as contributions from the Nb stripper foil (f_{target}).

1. Number of primary projectiles

The number of impinging projectiles on the production target was measured using a secondary electron transmission monitor (SEETRAM) [27] placed upstream of the target. It consists of three thin Ti foils with total thickness of 13.6 mg/cm^2 which ensures negligible primary beam attenuation with a reaction probability of 0.1% for a 1000 MeV/u ^{208}Pb beam. The SEETRAM output signal per spill, N_{SEETRAM} was calibrated against a plastic scintillator to determine the conversion factor between the signal and the true intensity of the beam. The uncertainty of the beam intensity measurement is 10%. The total number of primary particles on the Be production target was 3.63×10^{12} for the ^{203}Ir setting and 4.63×10^{13} for the ^{202}Os setting.

2. Electron capture and loss processes

The measured production cross sections reported in this work were evaluated for the ions that traversed the separator as fully ionized nuclei (the 0e-0e state in Sec. II A) and were fully ionised in at least one of the MUSIC detectors at F4. The correction factor f_q accounts for the fraction of ions that did not fulfill this condition.

The charge-state distributions in the MUSICs were experimentally determined from the measured data, whereas the fraction of fully ionized ions in the spectrometer was calculated with the GLOBAL model [28]. For a few nuclides, experimental data on the charge-state combinations 1e-0e or 0e-1e were available and were found to agree with the GLOBAL predictions within 3%. The factor f_q depends on the nuclear charge Z and varied from 1.21 ± 0.10 for $Z = 74$ to 1.45 ± 0.13 for $Z = 78$.

3. Ion-optical transmission

The transmission losses caused by geometric restrictions of the FRS apertures and by nuclear reactions of the fragments in the materials along the beam path were calculated using the Monte Carlo code MOCADI [29]. The simulation was based on a realistic ion-optical model of the FRS, in which each element (magnets, drift spaces, apertures, vacuum pipe, slits, etc.) was represented by its individual transfer matrix and its physical, i.e., mechanical, apertures. The calculated phase-space distributions were validated by comparison with the measured position and angular distributions of individual fragments at the focal planes F2 and F4. For the centered fragment, the simulated ion-optical transmission was 99.9%. No cross sections were evaluated for nuclides with a calculated ion-optical transmission below 10%.

For isotones with $N = 127$, a transmission calculation was not directly possible with the current version of MOCADI since charge-exchange reaction mechanism is not modelled in the code. Therefore, the kinematics of the $N = 127$ isotones were assumed to deviate from the Morrissey systematics [30]

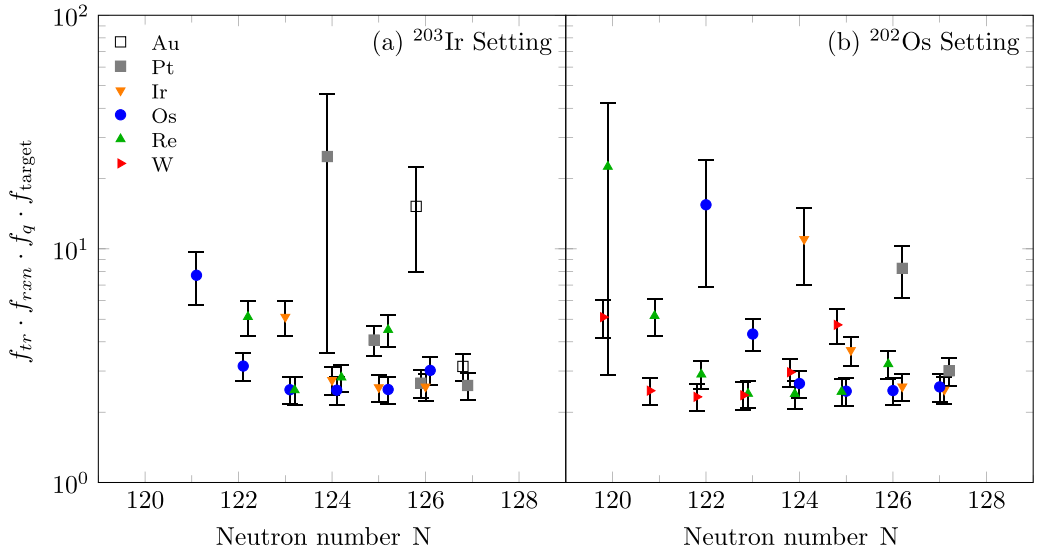


FIG. 5. Combined correction factor ($f_{tr} \cdot f_q \cdot f_{rxn} \cdot f_{\text{target}}$) as a function of neutron number for (a) ^{203}Ir setting and (b) ^{202}Os setting, note the log scale. The time-dependent factors f_{DAQ} and f_{det} are not shown here. See Secs. II B 2–II B 6 for details.

as reported by Morales *et al.* [31], and the transmissions for these isotones were then estimated by an interpolation based on the calculated transmissions of neighboring nuclides.

4. Reaction losses in the degrader and other pieces of matter traversed by the fragment beams

As the ions traversed the separator, they underwent reactions in the material in the beamline (windows, detectors and degraders). These reaction losses were determined by using the Kox parametrization [32] of the total nuclear reaction cross sections for the fragment in each layer as implemented in the MOCADI code. In the experiment, an Al degrader with a thickness of 4500 mg/cm^2 was used at F2. This degrader constituted the dominant contribution to the secondary reaction losses, accounting for around 60% of the total reaction probability. Each fragment was treated individually and the total reaction probability for each of them was of about 0.5 leading to $f_{rxn} \approx 2.0$.

5. Nuclear reactions in the Be/Nb production target

The measured yield for a given nuclide includes contributions from both direct production from the primary-beam-target interaction but also from multistep reactions of primary fragments within the target material before they exit the target. This probability was calculated using the LISEcute + + software (version 17.12.21) by modeling the complete reaction and attenuation within the target [33]. The production cross sections for both the primary-beam-target and fragment-target reactions were parameterised using EPAXv3.1 [34]. On average the simulation predicted that the measured yields increase by approximately 2% for the reported fragments.

In addition, the contribution from the Nb stripper to the measured yields was determined using EPAXv3.1 production cross sections and the Kox parametrization for total reaction cross sections within the MOCADI framework [29,32,34]. Under the present experimental conditions, the stripper contribution was approximately 1% and nearly constant for the investigated fragments. The quantity f_{target} accounts for both effects, multistep-production and contributions from the Nb foil to the total yield.

6. Aggregation of all contributions and cross section calculation

Finally, the individual production cross sections for the different nuclides were determined according to Eq. (2) combining all considerations and effects described before. While the first factor in that equation contains time and intensity dependent quantities, which are measured, the other four factors are not and they have been estimated through calculations as discussed above. Their products $f_{tr} \cdot f_q \cdot f_{rxn} \cdot f_{\text{target}}$ vary from 2.5 to 25 and are displayed together with their estimated uncertainties in Fig. 5 for every measured nuclide. Overall, the picture shows that – despite the logarithmic ordinate – the factors make a manageable contribution that is known with reasonably good accuracy. The different magnitude arises mainly from the different ion-optical transmission: a small transmission gives rise to a large adjustment factor and *vice versa*. In most cases, the experimental error is dominated by the systematic uncertainties of reaction losses, primary beam intensity and transmission, while in some cases, the error is dominated by the counting statistics. When a fragment is observed in both experimental settings (with an ion-optical transmission greater than 10%, as mentioned in Sec. II B 3), the reported cross section represents a weighted average of the two measurements.

III. RESULTS AND DISCUSSION

The measured production cross sections for neutron-rich nuclides near the $N = 126$ shell closure are presented in Table I alongside their total uncertainties, which combine both statistical and systematic contributions. Column labeled with 'Counts' gives the total number of observed events of the corresponding nuclide.

TABLE I. Measured production cross sections, σ, in mb in the reaction 1000 MeV/u ^{208}Pb + ^{9}Be. The errors include both systematic and statistical uncertainties. The column labeled with 'Counts' gives the total number of observed events (N_f) of the corresponding nuclide.

Z	N	A	$\sigma \pm \Delta\sigma$ (mb)	Counts
79	127	206	$(2.67 \pm 0.47) \times 10^{-4}$	26200
79	126	205	$(1.19 \pm 0.58) \times 10^{-2}$	241133
78	127	205	$(1.23 \pm 0.22) \times 10^{-5}$	5912
78	126	204	$(4.00 \pm 0.80) \times 10^{-4}$	193295
78	125	203	$(2.71 \pm 0.50) \times 10^{-3}$	206473
78	124	202	$(7.90 \pm 6.82) \times 10^{-3}$	97961
77	127	204	$(3.95 \pm 0.71) \times 10^{-7}$	562
77	126	203	$(1.87 \pm 0.33) \times 10^{-5}$	33266
77	125	202	$(1.27 \pm 0.22) \times 10^{-4}$	135315
77	124	201	$(5.53 \pm 1.10) \times 10^{-4}$	197147
77	123	200	$(1.83 \pm 0.37) \times 10^{-3}$	32170
76	127	203	$(7.23 \pm 2.61) \times 10^{-9}$	10
76	126	202	$(3.54 \pm 0.72) \times 10^{-7}$	937
76	125	201	$(4.54 \pm 0.80) \times 10^{-6}$	8694
76	124	200	$(2.99 \pm 0.52) \times 10^{-5}$	47324
76	123	199	$(1.19 \pm 0.21) \times 10^{-4}$	111773
76	122	198	$(3.58 \pm 0.69) \times 10^{-4}$	91806
76	121	197	$(9.14 \pm 2.54) \times 10^{-4}$	37440
75	126	201	$(9.96 \pm 3.49) \times 10^{-9}$	11
75	125	200	$(1.29 \pm 0.28) \times 10^{-7}$	263
75	124	199	$(1.10 \pm 0.20) \times 10^{-6}$	2222
75	123	198	$(5.76 \pm 1.02) \times 10^{-6}$	11711
75	122	197	$(2.65 \pm 0.49) \times 10^{-5}$	37388
75	121	196	$(7.63 \pm 1.62) \times 10^{-5}$	52954
75	120	195	$(1.38 \pm 1.21) \times 10^{-4}$	21712
74	125	199	$(6.66 \pm 3.27) \times 10^{-9}$	5
74	124	198	$(4.43 \pm 0.99) \times 10^{-8}$	53
74	123	197	$(2.99 \pm 0.54) \times 10^{-7}$	449
74	122	196	$(1.41 \pm 0.25) \times 10^{-6}$	2156
74	121	195	$(5.31 \pm 0.93) \times 10^{-6}$	7627
74	120	194	$(1.45 \pm 0.31) \times 10^{-5}$	10112

The present work identified fragments within the $Z = 74$ to $Z = 79$ range and measured the production cross sections of 31 neutron-rich nuclides, including four $N = 127$ nuclides. The first production cross section measurements were performed for nine nuclides: ^{196}W, ^{197}W, ^{198}W, ^{199}W, ^{199}Re, ^{200}Re, ^{201}Re, ^{202}Os, and the $N = 127$ nuclide ^{203}Os from the fragmentation of ^{208}Pb in a beryllium target.

From the data shown in Table I, the decline of production cross sections with increasing neutron number is evident. The smallest cross sections measured in the present experiment reach down to the level of ≈10 pb. It is also evident that the cross sections for reactions leading to nuclides with neutron number $N = 127$ – one neutron more than the primary beam – decrease significantly faster than the general trend when compared to $N = 126$ isotope of the same element. The reason for this is the different reaction processes that lead to the respective nuclides. The following discussion is divided into three parts: fragmentation reactions, the multiple-proton-removal channels yielding the $N = 126$ isotones, and charge-exchange reactions leading to fragments with $N = 127$. The present data will be compared with the predictions of model calculations and, where available, with literature data.

A. Comparison with the predictions of fragmentation models

Figure 6 shows the measured production cross sections for the elements from tungsten to gold. The data for the $N = 127$ nuclides are omitted from this figure because they are produced by a different reaction mechanism. The fragmentation data from Ref. [35], obtained for the same reaction 1000 MeV/u ^{208}Pb + ^{9}Be, are also shown. In general, the two data sets agree within a factor of two. The present data, however, extend the previously available measurements towards more neutron-rich isotopes of osmium, rhenium, and tungsten.

Projectile fragmentation occurs in peripheral nuclear reactions, leading to the removal of protons and/or neutrons from the projectile. Several semiempirical parametrizations and Monte Carlo models have been developed to predict production cross sections and to improve the understanding of the fragmentation process and its reaction kinematics. In order to evaluate and benchmark the predictive power of existing fragmentation models in the heavy neutron-rich region, the measured cross sections have been compared with results from several widely used models: the empirical parametrizations EPAXv2.15 [36] and EPAXv3.1 [34], the Monte Carlo abrasion-ablation code ABRABLA07 [37], its analytical version COFRAv26.04 [22,38], the Liège intranuclear cascade model (INCL + +v6.34) coupled to ABLA + +v25.08 for de-excitation [39,40], and the empirical parametrization FRACSv1.1 [41].

EPAX is a universal semiempirical parametrization based on the limiting-fragmentation hypothesis, i.e., that the yields of final fragmentation residues are independent of the initial kinetic energy of the projectile. As seen in Fig. 6, EPAXv3.1 systematically underestimates the measured cross sections by approximately one order of magnitude, and the discrepancy becomes more pronounced for the most neutron-rich nuclides. It reproduces the lower-mass fragments of rhenium and tungsten reasonably well, as shown in Figs. 6(e)–6(f). One of the modifications introduced in EPAXv3.1 was a downscaling factor that depends on the neutron excess of both the projectile and the fragment [34], implemented to better reproduce previously available experimental data, e.g., [42]. However, the data of the present work are in better agreement with the previous version EPAXv2.15.

ABRABLA07 is a two-stage Monte Carlo abrasion-ablation model. For the present comparison, 5×10^8 events were simulated, in order to calculate cross sections down to the order of 10^{-4} mb. Therefore, comparisons to smaller measured cross sections are not meaningful within the available simulation statistics. The calculated results and their corresponding statistical uncertainties are shown in Fig. 6. Overall, ABRABLA07 shows good agreement with the measured data.

COFRAv26.04 [38] is an analytical cold-fragmentation model that considers the abrasion of both protons and/or neutrons, followed by the evaporation of neutrons only during the ablation stage. The code, an improved version of the original COFRA code [22], now calculates reaction cross

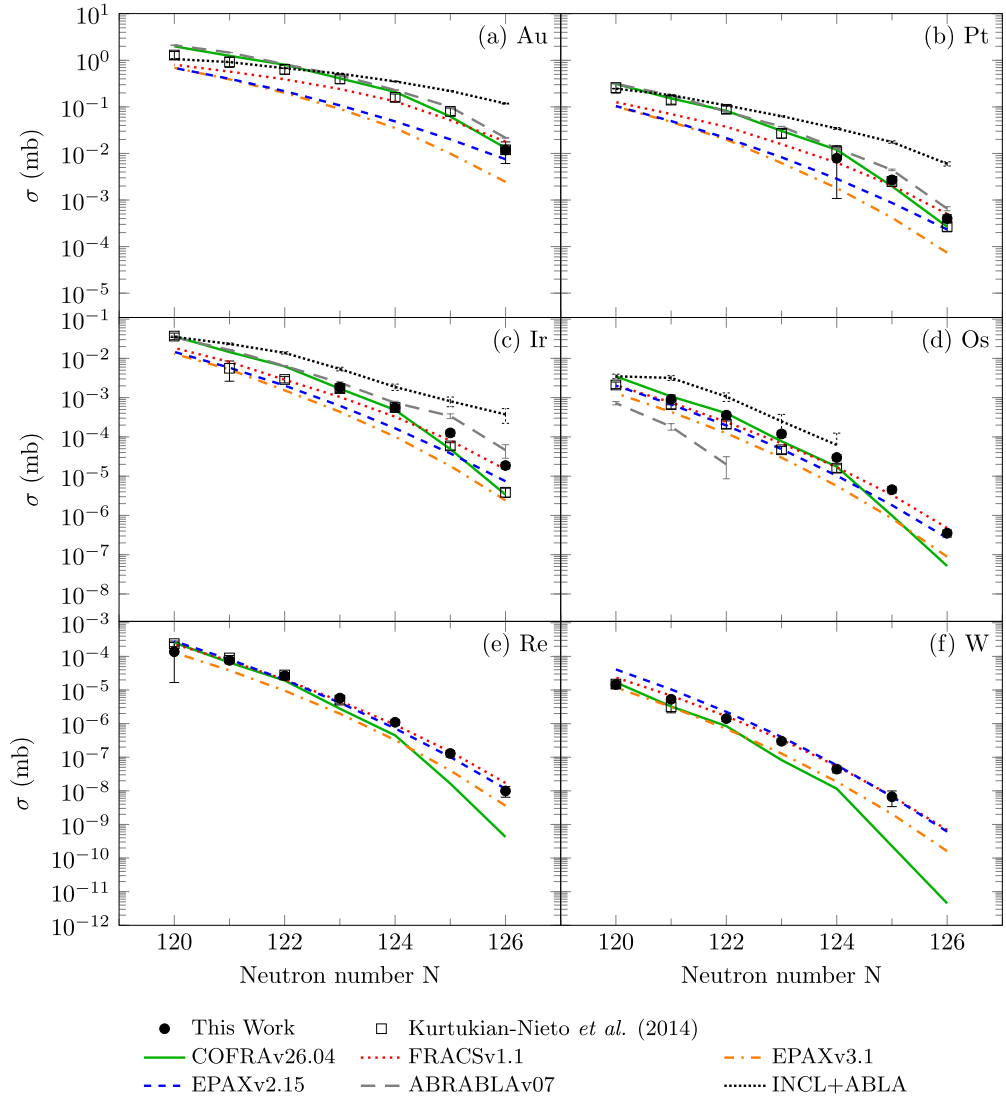


FIG. 6. Measured production cross sections of fragment residues from element $Z = 79$ to $Z = 74$ produced in the reaction 1000 MeV/u ^{208}Pb + ^{9}Be (filled black circles). Data from Kurtukian-Nieto *et al.* [35] obtained for the same reaction are also shown (open black squares). If the error bars of the experimental data are not visible, they are smaller than the marker size. The lines show predictions of various models: COFRAv26.04 calculation (solid green line) [22,38], FRACSv1.1 parametrization (red dotted line) [41], EPAXv3.1 parametrization (orange dashdotted line) [34], EPAXv2.15 parametrization (blue dashed line) [36] ABRABLA07 (gray long dashed line) [37], and INCL + ABLA (black double dot dashed line) [39,40].

sections according to the Karol model [43], incorporating the modifications introduced by Brohm and Schmidt [44]. It shows reasonable agreement for fragments near the projectile mass. However, for neutron-rich nuclides far from the projectile, it tends to underestimate the production cross sections.

A simulation with INCL + ABLA was performed with 1.5×10^8 events under strict Pauli blocking [45]. INCL + ABLA combines a microscopic intranuclear-cascade description of the initial collision stage with a statistical de-excitation model. In the region studied here, the model overestimates the production cross sections by up to a factor of twenty. At present, it is not clear whether this discrepancy originates primarily from the INCL + + or the ABLA + + component.

FRACSv1.1 is a next-generation empirical parametrization that includes a projectile-energy dependence as well as an odd-even staggering term for fragments with $A \leqslant 150$. It provides the best overall agreement with the experimental data, representing an improvement over the other models. All measured cross sections in the present work are reproduced within a factor of 1.8.

B. Multiple-proton-removal reactions

Cold fragmentation represents a special reaction process in which the projectile loses only protons during the initial abrasion stage, while the excitation energy remains below the neutron-evaporation threshold [22]. Consequently, multiple-proton removal can be an avenue to neutron-rich heavy nuclides, although the corresponding cross sections decrease exponentially with every removed proton.

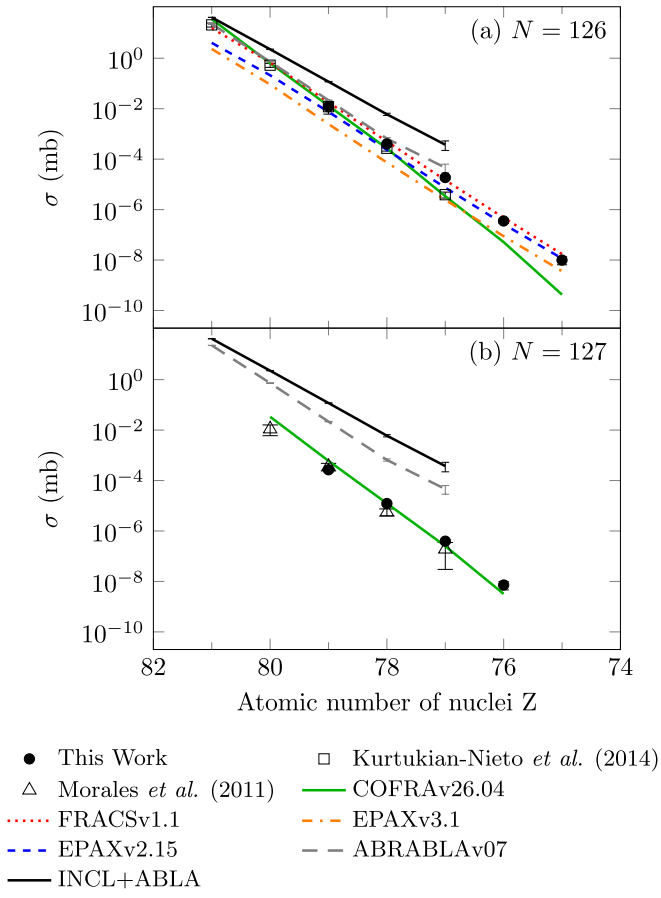


FIG. 7. (a) Production cross sections for the $N = 126$ isotones via proton removals, measured in the reaction 1000 MeV/u ^{208}Pb + ^{9}Be (filled black circles). The data are compared with literature Kurtukian-Nieto *et al.* [35] obtained for the same collision system and energy (open black square). The lines show predictions of various models: COFRAv26.04 calculation (solid green line) [22,38], FRACSv1.1 parametrization (red dotted line) [41], EPAXv3.1 parametrization (orange dashdotted line) [34], EPAXv2.15 parametrization (blue dashed line) [36], ABRABLA07 (gray long dashed line) [37], and INCL + ABLA (black double dot dashed line) [39,40]. (b) Production cross sections of $N = 127$ isotones in charge-exchange reactions: 1000 MeV/u ^{208}Pb + ^{9}Be (filled black circles; this work), 1000 MeV/u ^{208}Pb + ^{9}Be (open black triangle) from Morales *et al.* [31]. Line styles correspond to the same models as in panel (a). If the error bars of the experimental data are not visible, they are smaller than the marker size.

The proton-removal cross sections determined in the present experiment are shown in Fig. 7(a). They exhibit a clear exponential decrease, as expected from the tail of a hypergeometric probability distribution, which is used to describe the statistical abrasion of protons only. The data are compared with the predictions of the models discussed above. As already noted in Sec. III A, EPAXv3.1 underestimates the production cross sections, whereas EPAXv2.15 reproduces the cross sections for multiple-proton removal comparatively well. INCL + ABLA, as discussed above, overestimates the cross sections by up to factor of 20. COFRAv26.04 decreases too steeply as more protons are abraded, while ABRABLA07 tends to overpredict the cross sections. FRACSv1.1 reproduces the measured values very well up to seven-proton removal. Overall, FRACSv1.1 and EPAXv2.15 provide the best predictive power for the $N = 126$ nuclides across nearly nine orders of magnitude.

C. Charge-exchange reactions

The observation of nuclides with neutron number $N = 127$, i.e., with one more neutron than the primary-beam projectile, is only possible if neutrons are absorbed (which is kinematically extremely unlikely at the energies involved) or if a proton is converted into a neutron. In the present energy regime, this can occur through the excitation of a Δ resonance in the nucleus and its subsequent decay by the emission of a π^+ or π^0 [46]. The result of such processes was already observed for the same projectile-target-energy combination [31] and has been extensively discussed in Refs. [13,31,47] and references therein.

Figure 7(b) compares the present data with those from Ref. [31] and with the predictions of the suitable model predictions. In this case too, the present data go beyond the existing literature data and agree very well where available. Also here, the cross sections decrease exponentially with increasing number of removed protons over several orders of magnitude. Remarkably, the slope is very similar: the observed ratio of cross sections between isobaric neighbors with $(Z, N = 126)$ and $(Z - 1, N = 127)$ is on the order of 10^{-3}. This ratio can be understood in terms of a single nucleon-nucleon charge-exchange interaction occurring during the abrasion stage. In COFRAv26.04, the charge-exchange probability (P) is calculated according to

$$P = \left(\frac{Z}{A}\right)_{\text{proj}} \left[\left(\frac{N}{A}\right)_t \sigma_{pn}\left(\frac{1}{2}\right) + \left(\frac{Z}{A}\right)_t \sigma_{pp}\left(\frac{5}{12}\right)\right] \frac{1}{\sigma_{\text{R}}},$$

where σ_{R} is the total reaction cross section obtained according to Refs. [43,44]. The parameters σ_{pn} and σ_{pp} are the elementary inelastic proton (in the projectile)–neutron (in the target) and the elementary inelastic proton-proton cross sections [48], respectively, at the projectile energy, leading to Δ-resonance excitations in either the target or the projectile [46,47]. Both cross sections are weighted by the proton fraction of the projectile, $(Z/A)_{\text{proj}}$, and by the neutron and proton fractions of the target nucleus, $(N/A)_t$ and $(Z/A)_t$. The factors 1/2 and 5/12 account for the effective isospin weights of the pn and pp channels that lead to $(Z, N) \rightarrow (Z - 1, N + 1)$) in the projectile, respectively (see Ref. [49]). For the present reaction, this expression yields a probability of the order of 10^{-3}, in excellent agreement with the measured ratio between neighboring isobars. The production cross sections of the $N = 127$ isotopes are then obtained as $\sigma(Z - 1, N = 127) = P \times \sigma(Z, N = 126)$. This description is further supported by the very good agreement between the COFRAv26.04 predictions and the experimental data, as shown in Fig. 7(b). This may indicate that the formation of nuclides with neutron number $N = 127$ can be considered to be due to two independent processes: multiple-proton removal leading to a $N = 126$ prefragment and a single charge-exchange

interaction with a target nucleon both occurring during the abrasion stage.

IV. SUMMARY

Production cross sections of neutron-rich projectile fragments from the reaction of 1000 MeV/u ^{208}Pb + ^{9}Be have been experimentally determined using the high-resolution separator and magnetic spectrometer FRS. Nine new cross sections have been measured in the region tungsten to gold near the $N = 126$ neutron shell closure. Through multiple-proton-removal reactions, this experiment extends previous measurements of $N = 126$ nuclides to ^{201}Re, which is produced via seven-proton removal, and of $N = 127$ nuclides to ^{203}Os, which is generated via five-proton removal and simultaneous charge-exchange reactions. The sensitivity of the measurement is approximately 10 pb. The measured production cross sections are well described by both EPAXv2.15 and FRACSv1.1 across the studied nuclides. Furthermore, COFRAv26.04 describes very well the production cross sections of $N = 127$ isotopes resulting from multiple-proton removal collisions, in which one of the nucleon-nucleon interactions involves a charge exchange. Thus these models offer reasonable estimates of secondary-beam intensities for future experimental studies in this region.

ACKNOWLEDGMENTS

The results presented here are based on the experiment S450, which was performed at the FRS with the DESPEC decay station at the GSI Helmholtzzentrum für Schwerionenforschung, Darmstadt (Germany) in the context of FAIR Phase-0 campaign. The authors thank B. Mei for FRACSv1.1 calculations. We thank P. Schwarz, T. Weber, B. Szczepanczyk, M. Will, and K.-H. Behr for excellent technical support, B. Lommel and B. Kindler and the GSI Target laboratory for providing high quality targets and degraders for the present experiment, and N. Kurz for continued support with the multibranch system (MBS) for the FRS data acquisition. This work was supported by Helmholtz Research Academy Hesse for FAIR (HFHF), HGS-HIRe and GET_INvolved Programme; the European Community Horizon 2020 – research and innovation programme, Contracts No. STRONG-2020 No. 824093; STFC (UK) (Grants No. ST/Y000358/1, No. ST/G000751/1, No. ST/G000697/1, No. ST/P005314/1, No. ST/V001108/1, No. ST/L005743/1, No. ST/P0005314, No. ST/P004598/1, No. ST/V001027/1, No. ST/Y000242/1, and No. ST/V001078/1); in part by the ExtreMe Matter Institute EMMI at the GSI Helmholtzzentrum fuer Schwerionenphysik, Darmstadt, Germany; the Slovenian Research and Innovation Agency (Grants No. I0-E005 and No. P1-0102); the Swedish Research Council (Vetenskapsrådet, VR 2022-3828); the MICIU/AEI/10.13039/501100011033, Spain with Project No. PID2023-150056NB-C42; BMBF/BMFTR 05P19RDFN1 GSI-TU Darmstadt cooperation contract; the Spanish Ministerio de Ciencia, Innovacion y Universidades (CNS2023-144871 and PID2023-150056NB-C41), Generalitat Valenciana (CISEJI/2022/25 and CIBEST/2024/219). J.L.R.-S. acknowledges support from the Xunta de Galicia under the program of postdoctoral fellowship No. ED481D-2021-018 and *Proyectos de excelencia*, Grant No. ED431F-2023/43, and from the *Ramón y Cajal* program under Grant No. RYC2021-031989-I, funded by MCIN/AEI/10.13039/501100011033 and by the "European Union NextGenerationEU/PRTR".

DATA AVAILABILITY

The data that support the findings of this article are not publicly available. The data are available from the authors upon reasonable request.

[1] M. Thoennessen and A. Gade, Isotope facilities aim to complete the nuclear chart, Nat. Phys. **20**, 1844 (2024).
[2] J. Erler, N. Birge, M. Kortelainen, W. Nazarewicz, E. Olsen, A. M. Perhac, and M. Stoitsov, The limits of the nuclear landscape, Nature (London) **486**, 509 (2012).
[3] I. Tanihata, H. Hamagaki, O. Hashimoto, Y. Shida, N. Yoshikawa, K. Sugimoto, O. Yamakawa, T. Kobayashi, and N. Takahashi, Measurements of interaction cross sections and nuclear radii in the light *p*-shell region, Phys. Rev. Lett. **55**, 2676 (1985).
[4] M. Pfützner *et al.*, First evidence for the two-proton decay of ^{45}Fe, Eur. Phys. J. A **14**, 279 (2002).
[5] R. Kanungo *et al.*, One-neutron removal measurement reveals ^{24}O as a new doubly magic nucleus, Phys. Rev. Lett. **102**, 152501 (2009).
[6] E. M. Lykiardopoulou, G. Audi, T. Dickel, W. J. Huang, D. Lunney, W. R. Plaß, M. P. Reiter, J. Dilling, and A. A. Kwiatkowski, Exploring the limits of existence of proton-rich nuclei in the $Z = 70$–82 region, Phys. Rev. C **107**, 024311 (2023).
[7] E. M. Burbidge, G. R. Burbidge, W. A. Fowler, and F. Hoyle, Synthesis of the elements in stars, Rev. Mod. Phys. **29**, 547 (1957).
[8] H. Geissel, G. Münzenberg, and K. Riisager, Secondary exotic nuclear beams, Annu. Rev. Nucl. Part. Sci. **45**, 163 (1995).
[9] H. Geissel and D. J. Morrissey, Exotic nuclei and their separation, electromagnetic devices, in *Handbook of Nuclear Physics*, edited by I. Tanihata, H. Toki, and T. Kajino (Springer, Singapore, 2023), pp. 3–61.
[10] T. Kubo, Recent progress of in-flight separators and rare isotope beam production, Nucl. Instrum. Methods Phys. Res. B **376**, 102 (2016).
[11] J. Äystö, Overview of recent highlights at ISOL facilities, Nucl. Phys. A **805**, 162c (2008).
[12] R. Serber, Nuclear reactions at high energies, Phys. Rev. **72**, 1114 (1947).
[13] C. Gaarde, Isobar excitations in nuclei, Annu. Rev. Nucl. Part. Sci. **41**, 187 (1991).

[14] H. Geissel *et al.*, The GSI projectile fragment separator (FRS): A versatile magnetic system for relativistic heavy ions, Nucl. Instrum. Methods Phys. Res. B **70**, 286 (1992).

[15] B. Kindler, E. C. Ayik, A. Hübner, B. Lommel, J. Steiner, and V. Yakusheva, Surface and thickness measurement in the Targetlab of GSI, EPJ Web Conf. **229**, 02002 (2020).

[16] G. Bartram *et al.*, Structure of the semi-magic ^{203}Ir and ^{202}Os nuclei, Phys. Lett. B **880**, 140790 (2026).

[17] A. K. Mistry *et al.*, The DESPEC setup for GSI and FAIR, Nucl. Instrum. Methods Phys. Res. A **1033**, 166662 (2022).

[18] M. Pfützner, H. Geissel, G. Münzenberg, F. Nickel, Ch. Scheidenberger, K.-H. Schmidt, K. Sümmerer, T. Brohm, B. Voss, and H. Bichsel, Energy deposition by relativistic heavy ions in thin argon absorbers, Nucl. Instrum. Methods Phys. Res. B **86**, 213 (1994).

[19] V. Hlinka, M. Ivanov, R. Janik, B. Sitar, P. Strmen, I. Szarka, T. Baumann, H. Geissel, and W. Schwab, Time projection chambers for tracking and identification of radioactive beams, Nucl. Instrum. Methods Phys. Res. A **419**, 503 (1998).

[20] R. Janik *et al.*, Time projection chambers with C-pads for heavy ion tracking, Nucl. Instrum. Methods Phys. Res. A **640**, 54 (2011).

[21] B. Voss *et al.*, The scintillation-detector equipment of the GSI projectile — fragment separator, Nucl. Instrum. Methods Phys. Res. A **364**, 150 (1995).

[22] J. Benlliure, K.-H. Schmidt, D. Cortina-Gil, T. Enqvist, F. Farget, A. Heinz, A. R. Junghans, J. Pereira, and J. Taieb, Production of neutron-rich isotopes by cold fragmentation in the reaction ^{197}Au +Be at 950 A MeV, Nucl. Phys. A **660**, 87 (1999).

[23] E. Casarejos *et al.*, Isotopic production cross sections of spallation-evaporation residues from reactions of ^{238}U (1A GeV) with deuterium, Phys. Rev. C **74**, 044612 (2006).

[24] B. Fornal *et al.*, Effective charge of the $\pi h_{11/2}$ orbital and the electric field gradient of Hg from the yrast structure of ^{206}Hg, Phys. Rev. Lett. **87**, 212501 (2001).

[25] Zs Podolyák *et al.*, Proton–hole excitation in the closed shell nucleus ^{205}Au, Phys. Lett. B **672**, 116 (2009).

[26] S. J. Steer *et al.*, Single-particle behavior at $N = 126$: Isomeric decays in neutron-rich ^{204}Pt, Phys. Rev. C **78**, 061302(R) (2008).

[27] B. Jurado, K. H. Schmidt, and K. H. Behr, Application of a secondary-electron transmission monitor for high-precision intensity measurements of relativistic heavy-ion beams, Nucl. Instrum. Methods Phys. Res. A **483**, 603 (2002).

[28] C. Scheidenberger, Th. Stöhlker, W. E. Meyerhof, H. Geissel, P. H. Mokler, and B. Blank, Charge states of relativistic heavy ions in matter, Nucl. Instrum. Methods Phys. Res. B **142**, 441 (1998).

[29] N. Iwasa, H. Geissel, G. Münzenberg, C. Scheidenberger, Th. Schwab, and H. Wollnik, MOCADI, a universal Monte Carlo code for the transport of heavy ions through matter within ion-optical systems, Nucl. Instrum. Methods Phys. Res. B **126**, 284 (1997).

[30] D. J. Morrissey, Systematics of momentum distributions from reactions with relativistic ions, Phys. Rev. C **39**, 460 (1989).

[31] A. I. Morales *et al.*, Synthesis of $N = 127$ isotones through (p,n) charge-exchange reactions induced by relativistic ^{208}Pb projectiles, Phys. Rev. C **84**, 011601(R) (2011).

[32] S. Kox *et al.*, Transparency effects in heavy-ion collisions over the energy range 100–300 MeV/nucleon, Phys. Lett. B **159**, 15 (1985).

[33] O. B. Tarasov, D. Bazin, M. Hausmann, M. P. Kuchera, P. N. Ostroumov, M. Portillo, B. M. Sherrill, K. V. Tarasova, and T. Zhang, LISE$^{++}_{\text{cute}}$, the latest generation of the LISE^{++} package, to simulate rare isotope production with fragment-separators, Nucl. Instrum. Methods Phys. Res. B **541**, 4 (2023).

[34] K. Sümmerer, Improved empirical parametrization of fragmentation cross sections, Phys. Rev. C **86**, 014601 (2012).

[35] T. Kurtukian-Nieto *et al.*, Production cross sections of heavy neutron-rich nuclei approaching the nucleosynthesis r-process path around $A = 195$, Phys. Rev. C **89**, 024616 (2014).

[36] K. Sümmerer and B. Blank, Modified empirical parametrization of fragmentation cross sections, Phys. Rev. C **61**, 034607 (2000).

[37] J.-J. Gaimard and K.-H. Schmidt, A reexamination of the abrasion-ablation model for the description of the nuclear fragmentation reaction, Nucl. Phys. A **531**, 709 (1991).

[38] J. L. Rodríguez-Sánchez (private communication).

[39] A. Boudard, J. Cugnon, J.-C. David, S. Leray, and D. Mancusi, New potentialities of the Liège intranuclear cascade model for reactions induced by nucleons and light charged particles, Phys. Rev. C **87**, 014606 (2013).

[40] J. L. Rodríguez-Sánchez, A. Graña-González, J.-C. David, G. García-Jiménez, J. Hirtz, and A. Kelić-Heil, Exploring total fission cross sections of neutron- and proton-induced reactions of exotic nuclei at relativistic energies using the INCL − ABLA + + models, Phys. Rev. C **111**, 064606 (2025).

[41] B. Mei, Improved empirical parameterization for projectile fragmentation cross sections, Phys. Rev. C **95**, 034608 (2017).

[42] J. Benlliure *et al.*, Production of medium-mass neutron-rich nuclei in reactions induced by ^{136}Xe projectiles at 1 A GeV on a beryllium target, Phys. Rev. C **78**, 054605 (2008).

[43] P. J. Karol, Nucleus-nucleus reaction cross sections at high energies: Soft-spheres model, Phys. Rev. C **11**, 1203 (1975).

[44] T. Brohm and K.-H. Schmidt, Statistical abrasion of nucleons from realistic nuclear-matter distributions, Nucl. Phys. A **569**, 821 (1994).

[45] J. Cugnon and P. Henrotte, The low-energy limit of validity of the intranuclear cascade model, Eur. Phys. J. A. **16**, 393 (2003).

[46] J. L. Rodríguez-Sánchez *et al.*, Systematic study of $\Delta(1232)$ resonance excitations using single isobaric charge-exchange reactions induced by medium-mass projectiles of Sn, Phys. Rev. C **106**, 014618 (2022).

[47] J. L. Rodríguez-Sánchez *et al.*, Study of Δ excitations in medium-mass nuclei with peripheral heavy ion charge-exchange reactions, Phys. Lett. B **807**, 135565 (2020).

[48] B. J. VerWest and R. A. Arndt, NN single pion production cross sections below 1500 MeV, Phys. Rev. C **25**, 1979 (1982).

[49] M. Fernández Ordóñez, Peripheral collisions induced by ^{124}Xe and ^{136}Xe projectiles at relativistic energies, Ph.D. Thesis, Universidad de Santiago de Compostela, Santiago de Compostela, Spain, 2007, https://igfae.usc.es/~genp/academic/tesis/PhD_manuel.pdf (accessed on 10.08.2026).